Master's thesis

NTNU
Norwegian University of Science and Technology
Faculty of Natural Sciences
Department of Materials Science and Engineering

Astrid Harboe Puntervold

# Molecular Dynamics Simulation of the Graphite-Electrolyte Interface in Lithium-Ion Batteries

Master's thesis in Materials Science and Engineering
Supervisor: Sondre Kvalvåg Schnell
Co-supervisor: Øystein Gullbrekken and Dennis Meyer
June 2023

NTNU
Norwegian University of
Science and Technology

Astrid Harboe Puntervold

# Molecular Dynamics Simulation of the Graphite-Electrolyte Interface in Lithium-Ion Batteries

Master's thesis in Materials Science and Engineering
Supervisor: Sondre Kvalvåg Schnell
Co-supervisor: Øystein Gullbrekken and Dennis Meyer
June 2023

Norwegian University of Science and Technology
Faculty of Natural Sciences
Department of Materials Science and Engineering

NTNU
Norwegian University of
Science and Technology

# Abstract

Energy storage is key to enable efficient and reliable utilization of renewable energy sources. The global demand of lithium-ion batteries is expected an annual growth by around 33 % by 2030. Even though lithium-ion batteries are considered marked-leading, there are several challenges associated with them. The understanding of the interface between electrolyte and electrode are still limited, and surface properties are difficult to investigate by use of current experimental methods.

To gain more insight about the interface between the anode and the electrolyte in a lithium-ion battery, a computer model was constructed by use of molecular dynamics. The system was built by use of LAMMPS, a molecular dynamics simulator software. Resulting in a graphite structure combined with an EC-DEC electrolyte. The concentration of each of the electrolyte component was recorded, and density profiles were plotted.

The model showed stable and realistic behaviour, and can be considered as a good model for the anode-electrolyte interface in a lithium-ion battery. In this project the model was used for investigating density profiles. The results showed an excess concentration of electrolyte in the interface region. Especially ethylene carbonate and lithium ions was found in higher concentrations close to the graphite anode.

# Sammendrag

Energilagring er nøkkelen for å muliggjøre effektiv utnyttelse av fornybare energikilder. Prognoser viser at den globale etterspørselen etter litium-ion-batterier forventes en årlig vekst på rundt 33 % innen 2030. Selv om litium-ion-batterier anses som markedsledende, er det flere utfordringer knyttet til dem. Kunnskapen rundt mekanismene som finner sted rundt grenseflata mellom elektrolytt og elektrode er fortsatt begrenset. Overflateegenskaper er vanskelige å undersøke ved bruk av nåværende eksperimentelle metoder.

For å få mer kunnskap om overflaten mellom anoden og elektrolytten i et litium-ion-batteri, ble en datamodell konstruert ved bruk av molekylærdynamikk. Dette ble utført ved bruk av LAMMPS, en programvare for simulator for molekylærdynamikk. Prosjektet resulterte i en grafittstruktur kombinert med en EC-DEC elektrolytt. Konsentrasjonen for hver av komponentene i elektrolytten ble målt og det ble plottet tetthetsprofiler.

Modellen viste stabil og realistisk oppførsel, og kan betraktes som en god modell for anode-elektrolytt-grensesnittet i et litium-ion-batteri. I dette prosjektet ble modellen brukt for å undersøke tetthetsprofiler. Resultatene viste en overskuddskonsentrasjon av elektrolytt i grensesnittområdet. Spesielt etylenkarbonat og litiumioner ble funnet i høyere konsentrasjoner nær grafittanoden.

# Preface

The work presented in this report is a part of the course "TMT4920 - Materials Technology, Master's Thesis". The project have been performed during the spring of 2023 - for the Department of Materials Science and Engineering at NTNU. The overall aim was to investigate and obtain more information about the transport mechanisms at the anode-electrolyte interface in lithium-ion batteries.

I would like to specially acknowledge and thank my supervisor Sondre Kvalvåg Schnell and co-supervisor Øystein Gullbrekken. Sondre has developed an inspiring and innovative master project, and has inspired me by his genuine desire to solve the challenges associated with batteries. This thesis would not have been possible without great guidance from Øystein. He has been available at any time and for any problem during this period, which have saved me a lot of time and frustration.

# Table of Contents

# 1 Introduction

## 1.1 Background and Motivation

The world's energy demand is growing significantly, primarily driven by population growth, economic development and increased use of technology. Towards the shift against a more sustainable consumption, traditional energy sources, such as fossil fuels need to be replaced with renewable sources. As part of this energy storage is key to enable efficient and reliable utilization. Therefore, in line with the demand of energy, the global demand for battery is also rapidly increasing. The global demand of lithium-ion batteries is expected an annual growth by about 33 % by 2030 [1]. This implies a total demand of 4300 GWh in 2030, where mobility applications account for the main part.

### 1.1.1 Lithium-ion Battery

Lithium-ion batteries (LIB) currently dominates the marked, but to meet the increasing demand for energy storage, intensified research is required to improve their performance [2].

LIB consists of coupled Li-ion cells coupled in parallel, series or combined. A basic cell consists of to electrodes contacted by an electrolyte, an separator is placed between the two electrodes to avoid them from get in contact. During charging, electrons are released at he cathode (positive electrode) due to an electrical supply. The electrons move externally to the anode (negative electrode), while lithium ions moves through the electrolyte in the same direction. This reaction stores the external energy in the form of chemical energy. During discharge the opposite reaction occurs. Figure 1.1 illustrates the basic components and the operating principle. The half-reactions happening at the cathode and anode, during charging are shown in equation (1.1) and (1.2) respectively [3].

$$LiCoO_2 \rightarrow CoO_2 + Li^+ + e^- \tag{1.1}$$

$$C_6 + Li^+ + e^- \rightarrow LiC_6 \tag{1.2}$$

Equation (1.3) represents the overall reaction. Right to left during the charging, and left to right during discharge.

$$LiC_6 + CoO_2 \rightleftarrows C_6 + LiCoO_2 \tag{1.3}$$

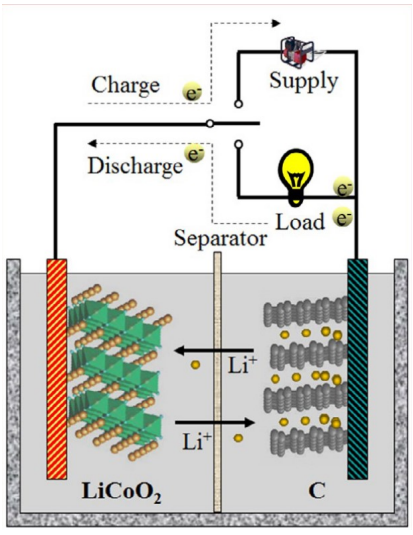


Figure 1.1: Illustration of a LIB battery [2].

In LIB the anode material is usually graphite. Graphite consists of a stack of graphene layers held together by weak van der Waals forces, with an interlayer distance of about 3.4 Å as shown in figure 1.2 [4]. The graphene structure is carbon atoms arranged in a hexagonal lattice, with interior angles of 120°. The carbon atoms are connected by strong covalent forces with bond lengths of 1.42 Å.

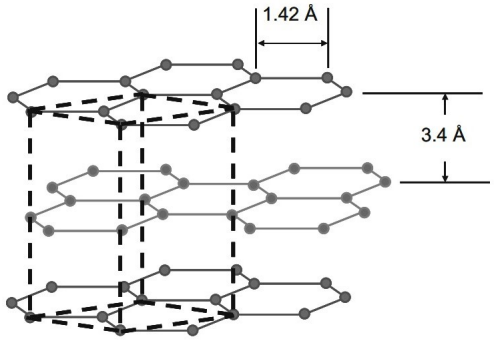


Figure 1.2: Schematic model of the layers in a graphite structure [4].

The LCO (Lithium-Cobalt-Oxide) and LFP (Lihium-Iron-Phosphate) are the most widely used commercal cathode materials today.

The electrolyte allows internal transport of lithium between the electrodes. The electrolyte is typically a lithium salt dissolved in an organic solvent. EC-DEC (1:1 w/w) + 1 M LiPF6 is an example of a commercial electrolyte, and is the one used in this project. It consists of ethylene carbonate (EC) and diethyl carbobonate (DEC) in a one-to-one weight ratio. The lithium salt in this electrolyte is a 1 molar lithium hexafluorophosphate solution.

## 1.2 Aim and Scope of the Work

When charging a LIB, lithium ions travel through an electrolyte and reaches the interface of the graphite anode. It is known that when the lithium reaches the interface, it meet a resistance to transport. In order to improve the performance of a LIB, this resistance need to be reduced. Current experimental methods can not characterize such thermodynamic- and kinetic surface properties, which makes molecular computational modelling highly valuable. Development of a good model of the graphite-electrolyte interface, can lead to new insights and useful discoveries about current and future challenges related LIBs.

# 2 Theory

## 2.1 Molecular Dynamics

Molecular Dynamics (MD) is a powerful computational method used to study equilibrium and transport properties of large systems [5]. It is used for simulating the motions of particles in the system based on specific algorithms. At the core of MD simulations are the interaction potentials between particles and the equations of motion that govern their dynamics [6].

By utilizing MD simulations, real experiments can be imitated and complex systems can be investigated [5]. An MD Simulation is initialized by defining a system of N particles. Bonded-and non-bonded forces are added and the system is equilibrated, which implies that Newton's equations of motion are solved until the system has reached a thermodynamic stable state. The model can then be used for further analysis.

In the following sections some basic algorithms and concepts relevant for this project is presented.

### 2.1.1 Time Integration and the Verlet-algorithm

Time integration in MD refers to the numerical method of computing the motion of a particle over time. The Verlet-algorithm is a basic technique for this integration [5]. It approximates the particle's position and velocity by using its previous position, velocity and the forces acting on it. The Verlet technique is derived form a Taylor expansion of the particle's coordinates. Consequently, it yields equation (2.1) for position and (2.2) for velocity. The method contains an error of order $dt^4$ for the position and $dt^2$ for the velocity [7].

$$r(t+\delta t) = 2r(t) - r(t-\delta t) + a(t)\delta t^2 \tag{2.1}$$

$$v(t) = \frac{r(t+\delta t) - r(t-\delta t)}{2\delta t} \tag{2.2}$$

A time stepping algorithm used in LAMMPS [8], is the Velocity Verlet-algorithm:

$$r(t+\delta t) = r(t) + \delta t v(t) + \frac{1}{2}\delta t^2 a(t) \tag{2.3}$$

$$v(t+\delta t) = v(t) + \frac{1}{2}\delta t[a(t) + a(t+\delta t)] \tag{2.4}$$

In addition to the previous position and velocity, Velocity Verlet uses the current acceleration. This does it more accurate than the Verlet method in some cases.

### 2.1.2 Thermostat and Barostat

Thermostats are applied in MD to control the temperature, like a heat bath in physical experiments [9]. This is done by adjustment of the velocities of the particles. By adjusting the velocities of the particles, the system gains or loses energy to maintain the desired temperature. The relation between temperature and velocities is a combination of the thermodynamic- and the classical expression for kinetic energy:

$$E_{kin} = \frac{3N}{2}k_B T = \frac{1}{2}mv^2 \tag{2.5}$$

where N = number of particles, $k_B$ = Boltzmann constant, T = temperature, m = particle mass and v = velocity of the particles.

Nose-Hoover thermostat is a canonical ensemble thermostat commonly used in MD. A canonical also called NVT ensemble implies that number of particles, volume and temperature are maintained constant. In this thermostat a friction variable is introduced to accelerate the particles to the desired temperature [9].

Barostats are applied in MD to control the pressure in the system. This is done by adjusting the volume of the system by different techniques.

The NPT, or isothermal-isobaric esnsemble is most used in MD. NPT requires that both kinetic energy and instantaneous pressure fluctuate in accordance with following function [10]:

$$f(x,V) = \frac{1}{N!V_0h^{3N}} \frac{exp[-\beta(H(x)) + PV)]}{\triangle(N,P,T)} \tag{2.6}$$

where P = the applied external pressure, V = system volume and T is the external pressure. $\beta = 1/kT$, x = phase-space vector, H(x) is the Hamiltonian system, $V_0$ = reference volume, and h is Plank's constant. The quantity $\triangle(N,P,T)$ is the partition function of NPT:

$$\triangle(N,P,T) = \frac{1}{N!V_0h^{3N}} \int_0^\infty dV \int dx\ exp[\beta(H(x) + PV)] \tag{2.7}$$

In MD, both thermostats and barostats is dependent of a relaxation constant. This parameter determines how rapidly the temperature is relaxed, given in in time units [11]. A relaxation constant of x will relax the temperature or pressure in a timespan of x time units.

### 2.1.3 Force Fields

Force fields in MD are essential to approximate interactions between particles within a system and determine its behaviour. These interactions includes both bonded- and non-bonded forces. The combination of forces can be expressed by the following equation:

$$E_{total} = \sum_{bonds} E_{stretch} + \sum_{angles} E_{bend} + \sum_{dihedrals} E_{torsion} + \sum_{impropers} E_{oop} + \sum_{pairs} E_{non-bond} \tag{2.8}$$

The energy related to bond stretching, $E_{stretch}$ can be described using a harmonic pair potential equation:

$$E_{bond} = \sum_{bonds} K_r(r - r_{eq})^2 \tag{2.9}$$

where r = distance between two atoms, $r_{eq}$ = equilbrium bond distance, and $K_r$ = Force constant.

The energy related to bond angle bending, $E_{bend}$ is related to the angle formed by two bonds. his energy can be quantified using a harmonic angle potential:

$$E_{angle} = \sum_{\theta} K_\theta(\theta - \theta_{eq})^2 \tag{2.10}$$

$\theta_{eq}$ = angle at equilibrium and $K_\theta$ = constant also describing the angular dependence.

The energy related to torsional forces, $E_{torsion}$, can be represented by a Fouriers series:

$$E_{torsion} = \frac{1}{2}K_1(1 + cos(\phi)) + \frac{1}{2}K_2(1 - cos(2\phi)) + \frac{1}{2}K_3(1 + cos(3\phi)) + \frac{1}{2}K_4(1 - cos(4\phi)) \tag{2.11}$$

The fourier coefficients K, represents the energy of the dihedral angles in the molecule. The

$E_{oop}$ is the energy related to displacement of atoms out of the plane. It can be described using a harmonic potential equation:

$$E_{oop} = K_\psi(\psi - \psi_0)^2 \tag{2.12}$$

where $\psi$ = angle between the two planes consisting of three atoms each (illustrated in The 2.1) and $K_\psi$ = force constant.

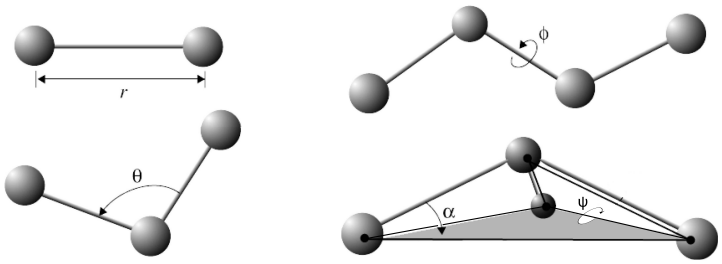


Figure 2.1: Bonds and angles related to bonded forces. Upper left: bond length, upper right: dihedral angle, lower left: bond angle and lower right: improper dihedral angle [12].

The non-bonded energy, $E_{non-bond}$, are related to forces not directly connected by chemical bonds. This includes interactions such as Coulombic or van-der-Waal-forces.

The Van der Waals forces are typically quantified by the Lennard-Jones model, which is described the interaction between non-bonded atoms: [6]:

$$V(r) = 4\epsilon[\Big(\frac{\sigma}{r}\Big)^{12} - \Big(\frac{\sigma}{r}\Big)^{6}] \tag{2.13}$$

where V = intermolecular potential between two non-bonded atoms, $\epsilon$ = measure of strength of the attraction between them, $\sigma$ = distance where the intermolecular potential between them equals zero, and r = distance between the atoms. The Lennard Jones potential and how the variables in equation (2.13) are related. is illustrated in 2.2.

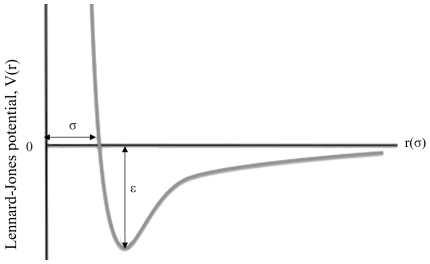


Figure 2.2: Typical curve for Lennard-Jones potential. The x-axis shows the distance between atoms, and y-axis the intermolecular potential. $\sigma$ represents the distance where the potential between the two atoms is zero, and $\epsilon$ is a measure of the attraction force between them.

Coulombic forces are governed by Coulombs law. This forces refer to the electrostatic forces between charged particles. These forces are typically calculated by following equation [13]:

$$V(r) = \frac{q_i q_j}{r_{ij}} \tag{2.14}$$

q in equation (2.14) is the charge of the particle and r is the distance between them.

## 2.2 Thermodynamics

### 2.2.1 Diffusion

Diffusion is often a rate limiting process and occur in all chemical mixtures [14]. The simplest description of diffusion of on component in another is given by Fick's law. The flux of one component in a system, is related to the gradient of its concentration:

$$J = -D\frac{dc}{dx} \tag{2.15}$$

where D = diffusion coefficient, c = concentration and x = position.

The diffusion of one component can be influenced by the concentration gradients of other components in a system [14]. This leads to a coupling of fluxes, which can be described by the Maxwell-Stefan equations.

The Maxwell-Stefan equations for a multicomponent system of n species, can be expressed as [15]:

$$d_i = \sum_{j=1}^{n} \frac{(x_i J_i - x_j J_i)}{c_i D_{ij}} \tag{2.16}$$

where x= positions, J = diffusion flux, x= consentration and D = Maxwell-Stefan binary diffusion coefficient.

The Maxwell-Stefan diffusion coefficients are defined from the Onsager relations which are important in explaining non-equilibrium thermodynamics. Non-equilibrium thermodynamics includes coupling of transport of heat, mass and charge, which are important in fully understanding of transport mechanisms in battery systems.

### 2.2.2 Interfaces

Heterogeneous systems have have an interfacial region that separates homogeneous phases. An interface is defined as "the thin layer between two homogeneous phases" [14]. A surface influences the thermodynamic properties of a system, and by use of Gibbs method in the form of "surface excess densities", they can be defined. To consider a system with an interface, it can be divided into three parts, two bulk phases and the interface between them. This is illustrated in figure 2.3.The figure shows how the entropy flux changes crossing a surface of thickness, $\delta$, which is small compared to the adjacent phases on both sides of the dotted lines. The notation $\sigma$, represents he excess surface entropy, $J_s^i$ and $J_s^o$ are the entropy fluxes in- and out of the surface respectively.

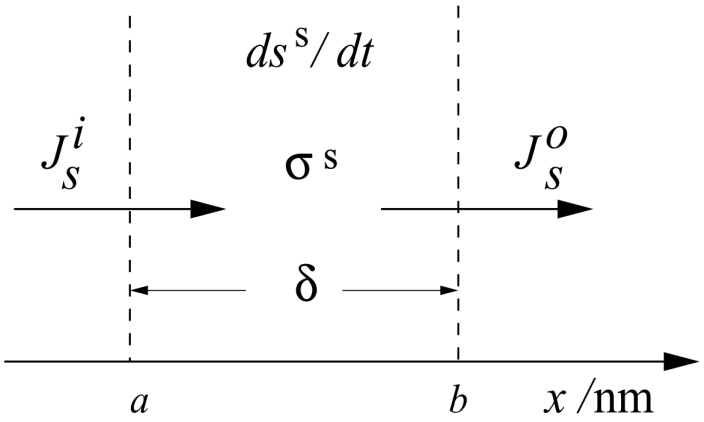


Figure 2.3: Entropy fluxes in and out of a surface of thickness $\delta$ = ba, leading to an excess surface entropy density, $\sigma^s$ [14].

Figure 2.4 shows an example of how the concentration of a substance B varies across the surface. The integral (shaded area) represents the excess surface concentration. This can be calculated by following expression for the excess surface consentration:

$$c^{exc} = \int [c(x) - c^A(x)\ \theta\ (x - x^s) - c^B(x)\ \theta\ (x^s - x)]dx \tag{2.17}$$

The excess density, $c^{exc}$, in (2.17), is given in moles per unit of surface area. It is a function of position x, the notations A and B represents the bulk-phases, $x^s$ is the position of the dividing surface. $\theta$ is the Heaviside function, which equals one when the argument ($x - x^s$ or $x^s - x$) is positive, and zero when the argument is negative. Simplified, the excess density is the difference between the density of a substance at the interface and the density of the same substance in the bulk.

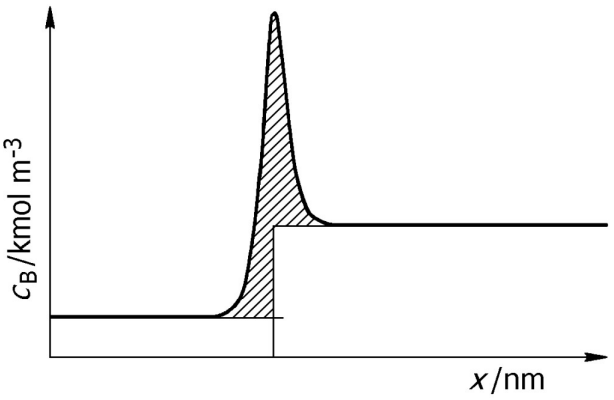


Figure 2.4: Concentration variation of a component B across a surface. Excess density of B is the integral illustrated by the shaded area. The vertical axis represents the position in nm, and the concentration is given in number density at the horizontal axis [14].

The interface in a system of an electrode and electrolyte has an highly inhomogeneous distribution of the chemical species [16]. The region where there exists strong interactions between ions and molecules in the electrolyte and the electrode surface is called the electrical double layer (EDL) [17]. Ions are attached to the electrode surface to balance the charge, and results in two layers of charge known as the EDL.

In LIBs, electrolyte reduction at the anode leads to a solid-electrolyte interface (SEI) [18]. The SEI consists of an inner layer (near the electrode) of inorganic compounds, and and outer layer (near the electrolyte) of organic compounds. The SEI layer is important for avoiding dendrite growth and obtain fast ion transport. In terms of reduction, EC is an important component in the electrolyte [19]. The binding energy of Li+ an EC is high and in the SEI layer one lithium ion is typically surrounded by 4-5 EC molecules.

### 2.2.3 Heat- and Mass Fluxes

In electrodes, there exist a large coupling between the transport of heat, mass and charge [14]. To explain these relations non-equilibrium thermodynamics is needed.

From the non-equilibrium definition of for entropy production[14], for fluxes of heat and mass can be derived and combined with the so called Onsager relations. All of the relations are explained in reference [14]. In relation to this project following expressions for heat- and mass fluxes could be relevant for further analysis:

$$J_q^{'} = l_{qq}\frac{\delta}{\delta x}\left(\frac{1}{T}\right) + l_{q\mu}\left(-\frac{1}{T}\frac{\delta}{\delta x}\mu_{1,T}\right) \tag{2.18}$$

$$J = l_{\mu q}\frac{\delta}{\delta x}\left(\frac{1}{T}\right) + l_{\mu\mu}\left(-\frac{1}{T}\frac{\delta}{\delta x}\mu_{1,T}\right) \tag{2.19}$$

The Onsager relations states that $l_{q\mu} = l_{\mu q}$. By use of constant temperature (T) or chemical potential ($\mu_{1,T}$), the expressions are further simplified and by experimentally measure the heat- and mass fluxes, it is possible to determine the coupling between the fluxes (Onsager constants).

# 3 Method

The system was built, and the calculations were conducted by use of the molecular dynamics code LAMMPS [20]. LAMMPS is an acronym for for Large-scale Atomic/Molecular Massively Parallel Simulator and is a powerful open-source software used for simulating molecular dynamics. This software can model complex systems and study details that are challenging to observe in traditional laboratory experiments. This can be done on both single CPU cores and the largest supercomputers with accelerators, this make LAMMPS well-suited for simulating large systems [21]. It is a flexible code with a wide range of force fields and potentials, so a variety of materials can be simulated, and the code can be customized for specific needs. LAMMPS exhibits exceptional scalability, making it suitable for simulating large systems on both single CPUs and advanced supercomputers with accelerators. In this project the simulations were run IDUN [22], a supercomputer that allows simulation of large systems and long run times to produce as realistic results as possible. The following sections describes the construction of the system consisting of a graphite structure combined with an EC-DEC electrolyte. For analysing the systems behaviour, the visualisation software OVITO [23] was used.

## 3.1 System Construction

### 3.1.1 Graphite

Initially, one single layer of graphene was build. This was done by creating a simulation box of dimensions 12x15x1 Å with periodic boundary conditions. The spherical cut-off distance used was 14 Å. This implies that atoms closer than 14 Å interacts with each other [24]. A hexagonal lattice of carbon atoms was defined, forming a single layer of graphene. The periodic boundary conditions make the carbons connect across the simulation box, so it acts like an infinite layer of graphene. In figure 5a the graphene sheet is represented only by the bonds to illustrate that they cross he boundary. The complete sheet including both atoms and bonds is represented in figure 5b.

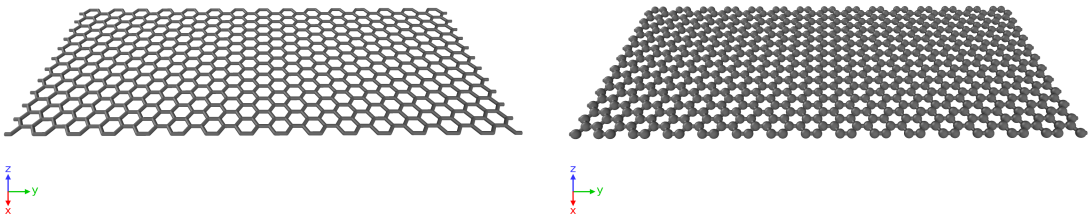


(a) (b)

Figure 5: Single layer of graphene (a) shows the bonds across the boundaries in y-direction and (b) shows both atoms and bonds

Hydrogen termination was performed by adding hydrogen-atoms manually to all the edge-carbons in the y-direction, the result is illustrated in figure (3.6). Termination is done to avoid the edge-carbons of forming new bonds.

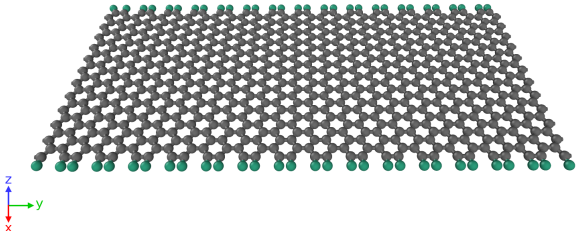

Figure 3.6: Terminated graphene sheet

Force field was applied by parameterization of both bonded- and non-bonded forces, corresponding to the variables found in the equations in section 2.1.3. The force field parameters used are given in appendix A. Figure 3.7 illustrates some of the relations existing in a graphene layer. In the relatively planar graphene layer, the improper dihedrals are difficult to visualize. To enhance visualization, the angle between the planes is magnified in the yellow box.

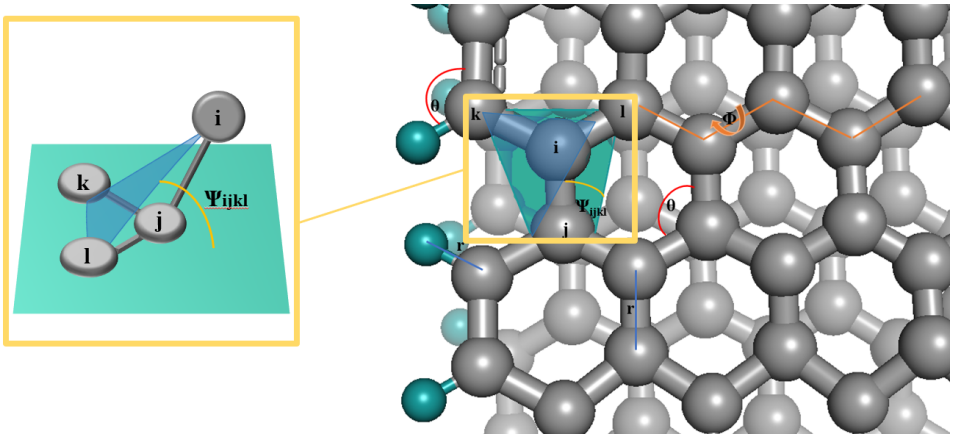


Figure 3.7: Some relations found in a layer of graphene. Blue lines show examples of bond distances, red ones - bonding angles, orange - a dihedral angle, and inside the yellow square - an improper dihedral [25].

To obtain the graphite structure, the terminated graphene sheet was replicated eight times in the z-direction. The result is shown in figure 3.8.

After complete construction of the graphite structure, energy minimizing was performed. Furthermore, the system was equilibrated in several steps. The target pressure during this steps was 1 atm and the target temperature 300 K. The relaxation constant was set to 100 for the temperature, and 1000 for the pressure. Initially, a Nose-Hoover thermostat was applied for 30 000 integration steps. To ensure proper stacking of the layers, a isobaric pressure of 1000 atm was applied in z-direction of for additional 30 000 steps. In the final equilibration step, an isothermal-isobaric barostat was applied for 10 000 000 integration steps. For equilibration of the graphite, a timestep of $1.0 * 10^{-}6$ nanoseconds was used.

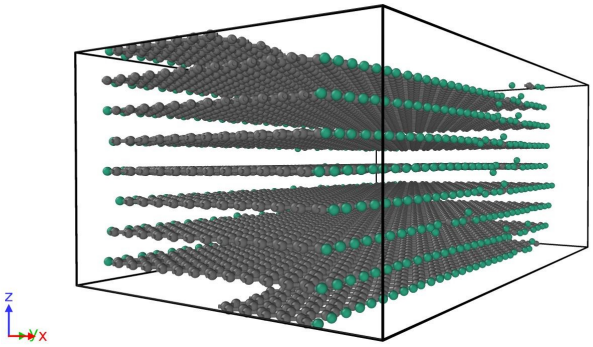


Figure 3.8: Graphite structure containing 8 layer of hydrogen terminated graphene.

To avoid translational motion of the mass center, that could cause the layers to move independently, the center-of-mass position was constrained. The bond lengths and angles for all atoms in the graphite was measured computationally and the interlayer distance between the graphene sheets were measured manually by use of Ovito.

### 3.1.2 Graphite-Electrolyte System

To prepare for the electrolyte the simulation box was extended in the x-direction, to make place for electrolyte at both sides of the terminated edges. Figure 3.9 shows how the graphite is structure surrounded by vacuum in x-direction.

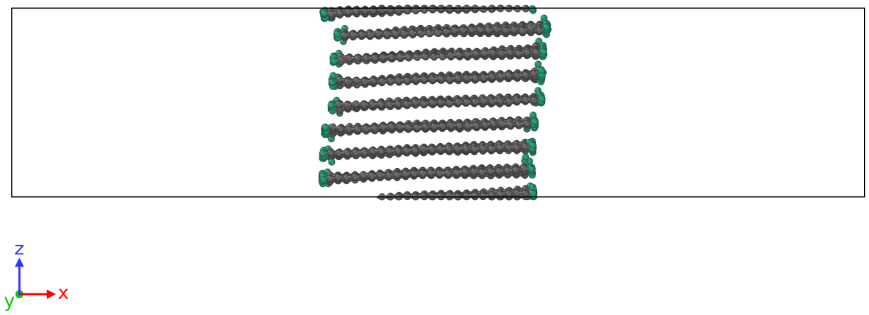


(a)

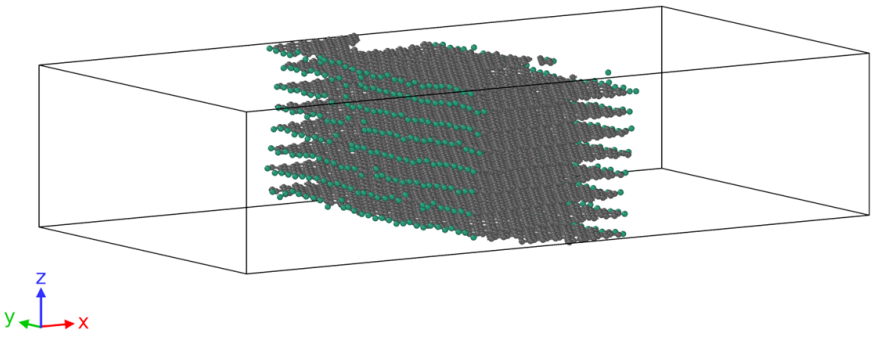


(b)

Figure 3.9: Simulation box expanded in x-direction.

A predefined EC-DEC electrolyte was put in the vakuum of the simulation box. The mass density of the bulk electrolyte was 1.200 $g/cm^3$, the composition is represented in table 1 and illustrated in fig 3.10 The simulation box was compressed in x-direction, with a pressure of 1000 atm, to remove the vakuum and create a better interface with the graphite. Thereafter, equilibration was performed by applying the Nose-Hoover thermostat with the same settings as before, but the timestep was reduced to $1.0 * 10^-7$ ns.

Table 1: Composition of EC-DEC electrolyte with a bulk mass density of 1.200 $g/cm^3$.

| Component | Number of molecules | Molar mass [g/mol] | Mole fraction |
|---|---|---|---|
| *EC* | 276 | 88.06 | 0.486 |
| *DEC* | 206 | 118.13 | 0.364 |
| *PF6-* | 46 | 144.96 | 0.081 |
| *Li+* | 46 | 6.94 | 0.081 |

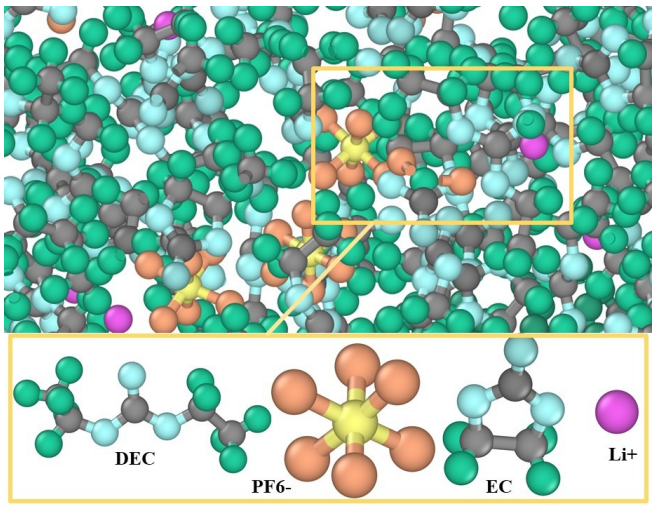


Figure 3.10: Visual representation of EC-DEC electrolyte and its components.

The procedure of combining graphite and electrolyte was performed three times, resulting in three parallels (1,2 and 3) with different initial distribution of the electrolyte. This was done to have a better representation and to improve the reliability of the result in the further analysis.

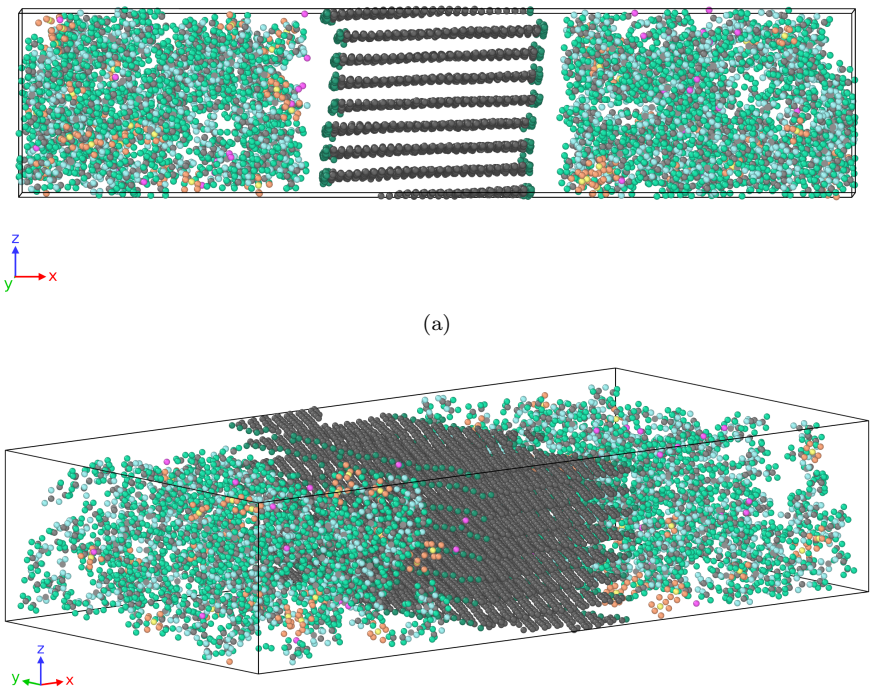


(a)

(b)

Figure 3.11: The combined system of graphite and EC-DEC electrolyte of the first parallel.

## 3.2 Density Calculations and Data Analysis

After the completion of the graphite-electrolyte system, density calculations were performed. The simulation box was separated into bins of 0.5 Å in x-direction, covering the whole box in the other two dimensions. Both number- and mass density were calculated. After obtaining "bulk" data, the bins were reduced to 0.05 Å and the densities for each of the chemical species of the electrolyte was recorded. Data was selected after a simulation time of 25 ns with a timestep of $5.0 * 10^{-}7$ ns.

After data collection, a isothermal-isobaric barostat was applied with target values of 300 K/1 atm and relaxation constants of 100/1000. The simulation time was 9.1 ns with timsteps of $5.0 * 10^{-}7$ ns. This step was added to investigate intercalation in the graphite.

# 4 Results and Discussion

In this section the stability and the quality of the constructed LIB model is evaluated. In addition results from the density calculations are presented and discussed.

## 4.1 Model Validation

### 4.1.1 Graphite

To evaluate and ensure that the system had reached equilibrium and force field. Parameters like bond length, angles and the interlayer distance in the graphite structured was measured, these are illustrated in figure 4.12 with corresponding values listed in table 2.

Table 2: Values for average bond lengths, angles and interlayer distance in the graphite structure

| *Parameter* | Value |
|---|---|
| *C-C bond length [Å]* | 1.41746 |
| *C-C-C angle [°]* | 119.913 |
| *Interlayer distance [Å]* | 3.40419 |

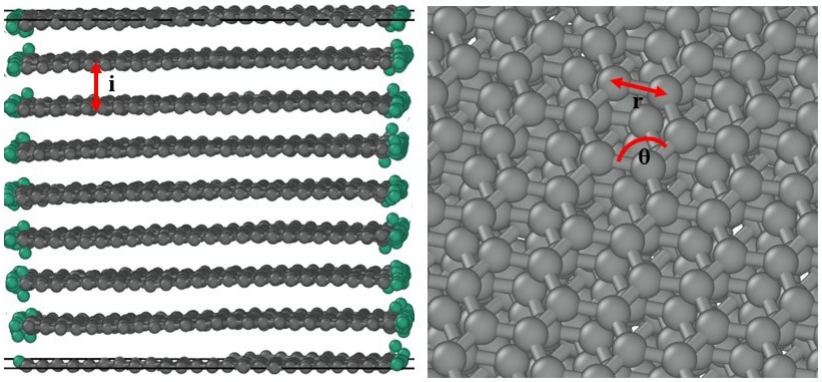


Figure 4.12: Bond length (r), angle ($\theta$) and the interlayer distance (i) in the graphite structure.

When comparing these values with theoretical values of carbon atoms in a graphite structure from section 1.1.1, it can be seen that the values corresponds well. The bond lengths and angles was determined by averaging measurements across the entire structure, without considering standard deviation or similar statistical measures. Regarding the interlayer distance, the value were obtained by averaging a random of measurements taken between the eight graphene sheets. It is possible to conduct more precise calculations, but the current method is adequate for excluding significant errors in the model. The bond lengths and angles for all atoms in the graphite was measured computationally and the interlayer distance between the graphene sheets were measured manually by use of Ovito.

To ensure that the graphite structure had reached a stable state after equilibration, values for temperature and potential energy was analysed. The results from the final equilibration of the graphite is graphically represented in figure 4.13.

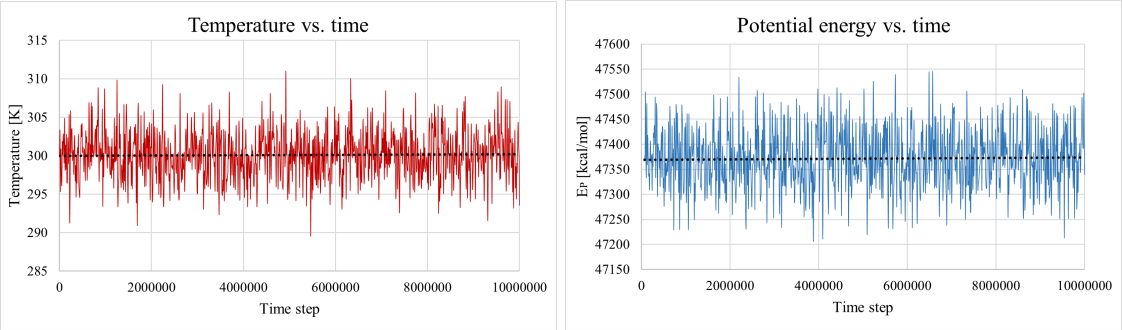


(a) (b)

Figure 4.13: NVT equilibration of graphite. The graphs shows how (a) temperature and (b) potential energy responds during equilibration of 10 ns.

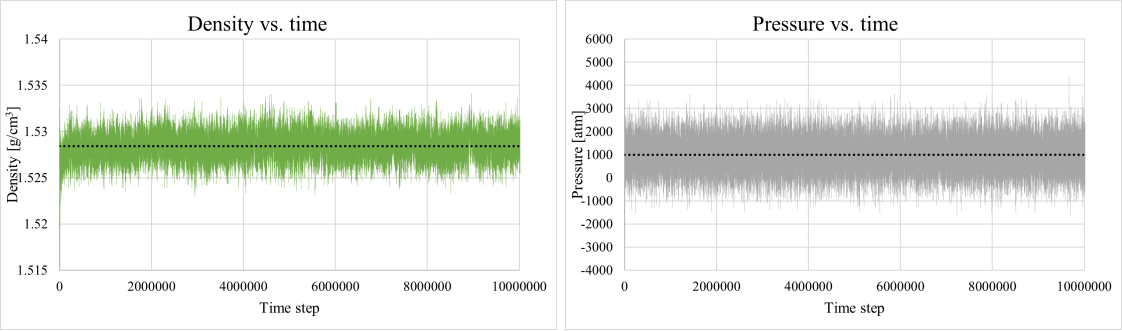


(a) (b)

Figure 4.14: NPT equilibration of graphite. The graphs shows how (a) density and (b) pressure responds during equilibration of 10 ns.

The trend lines of the graphs in figure 4.13 show that the temperature oscillates around the target of 300 K and the potential energy has stabilized with relatively small fluctuations. This indicates that the system had obtained an equilibrium condition. Figure 4.14 shows density- and pressure data during the compression process, ensuring that both variables have reached a stable state. Also observing the structure visually by use of Ovito, confirmed this evalution. The layers did not separate or move independently. The layers also remained rigid, and did not bend abnormally, figure 4.15 shows a clipping from Ovito after equilibration.

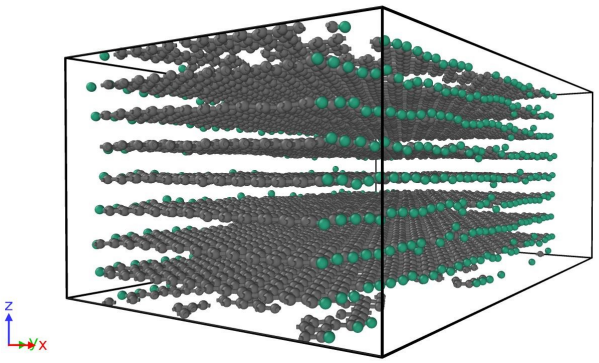


Figure 4.15: Hydrogen-terminated graphite structure after equilibration.

### 4.1.2 Graphite-Electrolyte System

To control if the system had reached a local potential energy minimum, the value in the second last time step was compared with the very last step of the minimization. Table 3 gives the energy values for the three parallels.

Table 3: Values from Energy Minimizing. Difference in energy (dE), between last ($E_n$) and second last ($E_{n-1}$) step should be small. $E_{initial}$ is the initial energy of the system.

| *System* | $E_{initial}[kcal/mol]$ | $E_{n-1}[kcal/mol]$ | $E_n[kcal/mol]$ | dE |
|---|---|---|---|---|
| *Parallel 1* | 52312.2450 | 40838.7048 | 40838.5125 | 0.1924 |
| *Parallel 2* | 52339.2523 | 40812.5114 | 40812.3614 | 0.1500 |
| *Parallel 3* | 52275.9388 | 40793.4578 | 40793.3134 | 0.1443 |

In relation to the initial energies, the change in energy, between the last two steps of the minimization was considered acceptable for all of the parallels. The most important result is nevertheless that the simulation did not crash during the energy minimizing. This indicates that the initial configuration of the system is physically reasonable and do not contain unrealistic atomic overlaps. Figure 4.17 shows the graphite-electrolyte system after equilibration. Comparing with figure 3.11 in section 3.1, it is observed that the system has been compressed in the x-direction, making the system tighter and the graphene layers more rigid due to the electrolyte "pressing" on both sides. This clippings are taken for simulation of parallel 1, but the same behaviour was observed also for parallel 2 and 3.

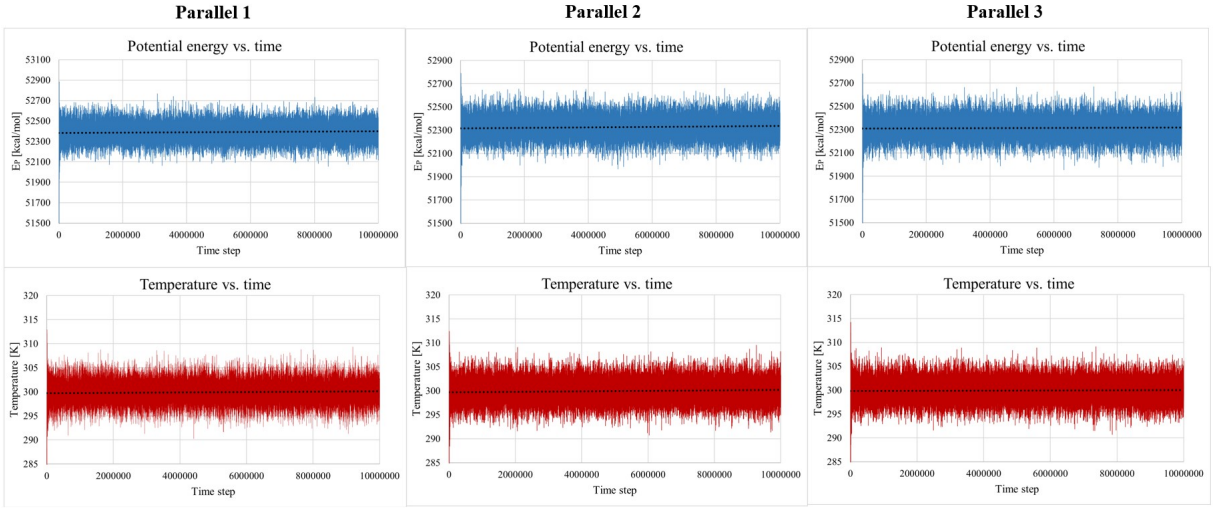


Figure 4.16: Potential energy and temperature for the three parallels during equilibration in the NVT ensemble.

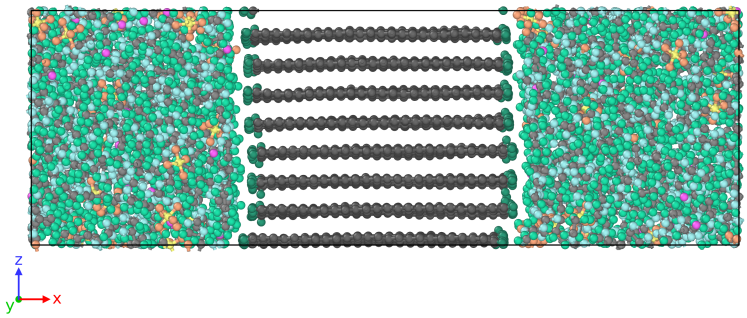


(a)

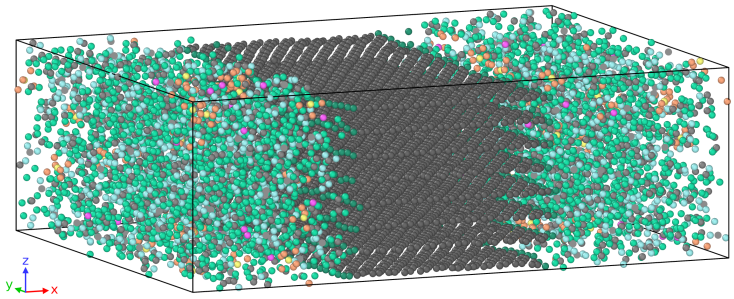


(b)

Figure 4.17: Combined system of graphite and electrolyte after equilibration.

## 4.2 Density Profiles

The density profile for the graphite-electrolyte system (bulk) is shown in figure 4.19. The mass per area (mass density) is quite stable at both edges. This is where the electrolyte is located. The average bulk concentration of the electrolyte (area is illustrated in figure 4.18), was calculated to a value of 1.136 $g/cm^3$, this differences 5.6 % from the theoretical bulk density of the electrolyte of 1.200 $g/cm^3$. This result can indicate that the bulk area of the system is slightly to small to give a accurate representation of the bulk electrolyte. The difference can still be considered acceptable, since there are no large fluctuations in this area (no gradient).

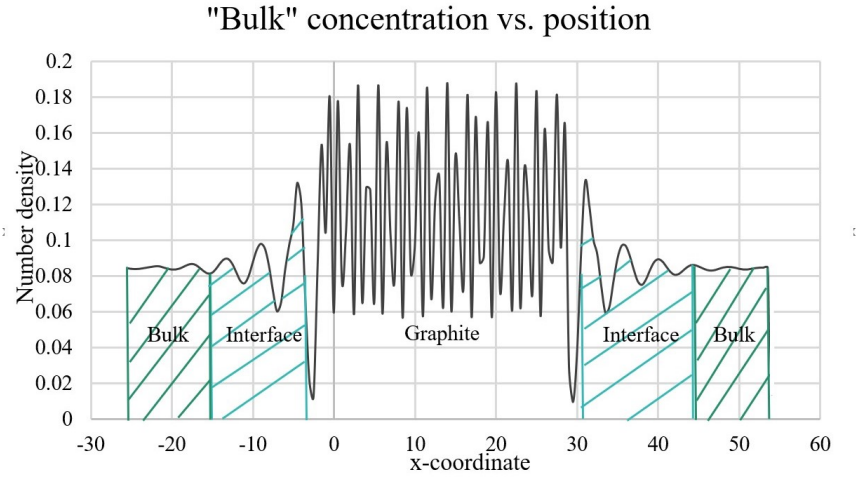


Figure 4.18: Illustration of areas used for calculating the concentrations in bulk and interface. The interface covers an area of about 10 Å on both sides of the graphite.

The bulk density was only measured for parallel 1, measurements of the two other parallels would have given more reliable results. The middle part of the graph represents the graphite structure, the large fluctuations are due to the space between the layers. Around 10 Å on both sides of the graphite, some larger peaks can be observed, this implies that the electrolyte concentration is higher in this area compared to the bulk-electrolyte. A ”gap” is observed at the edges of the graphite, indicating that there are no intercalation from the electrolyte into into the graphite. Since the density profiles were obtained by use of the central atom of the molecule, the gap will in reality, be narrower than illustrated by the graph. This is also observed visually in Ovito.

The data in this section is collected from a simulation of 50 million integration steps, a time step of 0.5 which corresponds to a simulation time of 25 ns.

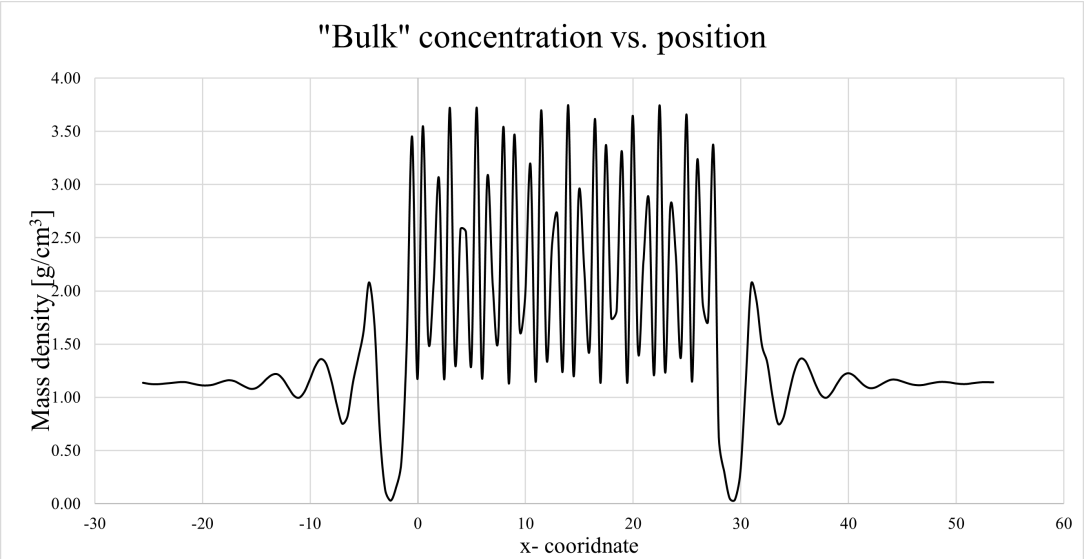


Figure 4.19: Density profile for bulk system of parallel 1.

The density profiles for Li+ and PF6- are plotted together in Figure 4.20. The densities of EC and DEC are plotted together in 4.21.

Higher density peaks of Lithium ions takes place near the graphite in both parallel 1 and 2. Parallel 3 has the largest peak at the left side, close to the graphite. For PF6-, there exists some larger peaks near the graphite, but in general they are mote randomly distributed compared to Li+.

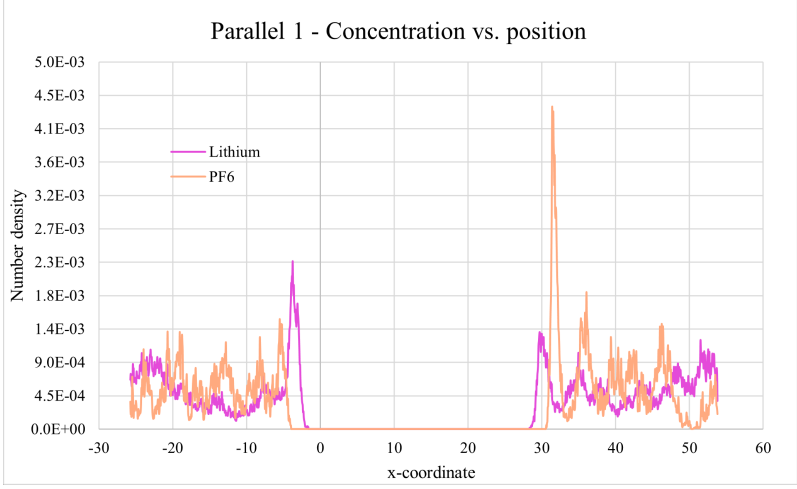


(a)

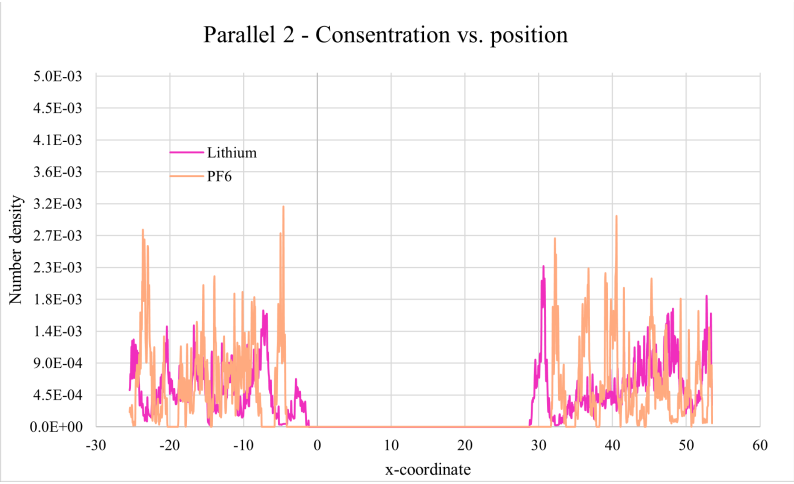


(b)

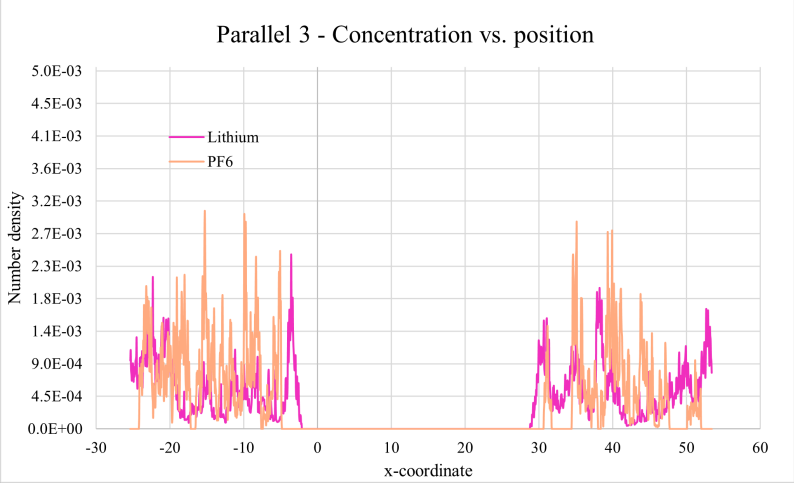


(c)

Figure 4.20: Density profiles for Li+ (pink curve) and PF6- (orange curve) (a) Parallel 1 (b) Parallel 2 (3) Parallel 3. Number density is given at the vertical axis, and the position of the simulation box in x-direction at the horizontal axis.

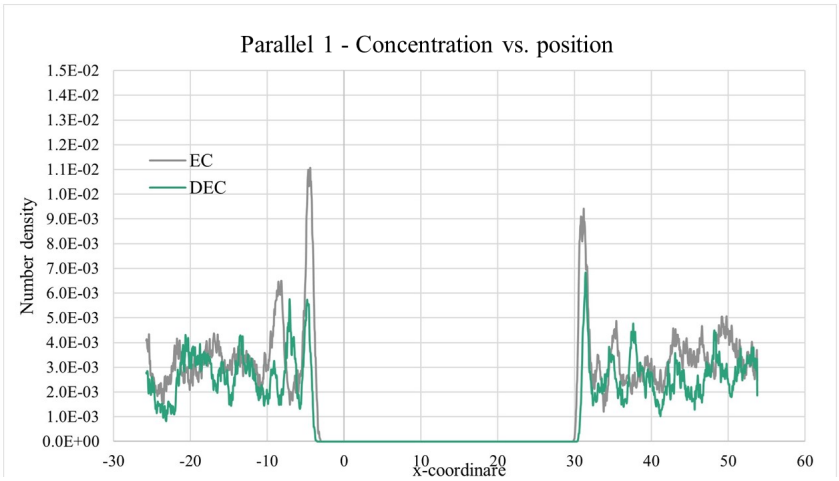


(a)

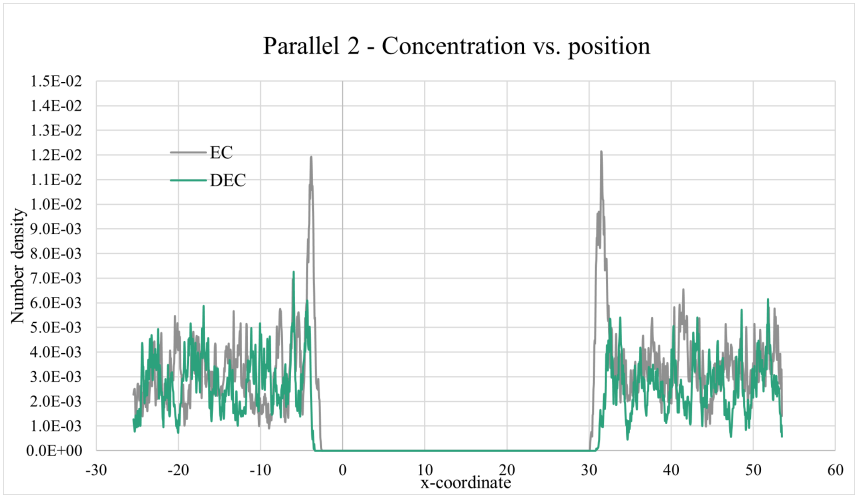


(b)

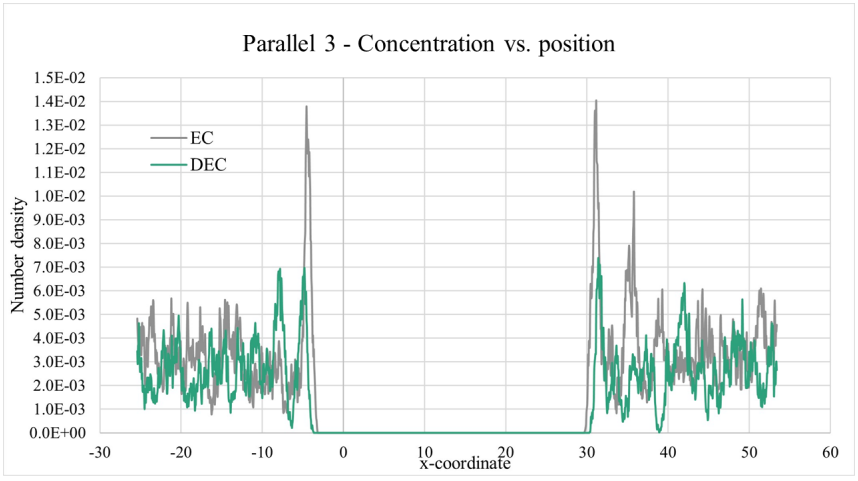


(c)

Figure 4.21: Density profiles for EC (grey curve) and DEC (green curve) (a) Parallel 1 (b) Parallel 2 (3) Parallel 3. Number density is given at the vertical axis, and the position of the simulation box in x-direction at the horizontal axis.

The density profiles of EC and DEC shows an even clearer trend of higher density peaks near the graphite. Especially the EC molecule, is found in high concentrations near the interface. The fact that the concentration near the interface is near the same as in the bulk, indicates that the

solvent is quite homogeneous. Some significant peaks are observed in the EC-concentration at the interface. Comparing with Li-concentration in figure 4.20, the positions of the peaks are located in the same area. This coexistence can be an indication of the SEI-layer reduction mentioned in section 2.2.2.

### 4.2.1 Excess Density

The surface excess concentration was calculated for the electrolyte in its entirety, and for each of the chemical species separately. The method used is described in section 2.2.2. The concentrations was calculated for both sides at the graphite. Figure 4.18 illustrates the areas used in the excess density calculations. The dividing surface was selected with an x-coordinate of -3.5 for the left side and 30.5 for the right side. The results of the excess concentration calculations for the three parallels are shown in table 4, 5 and 6.

Table 4: Excess Concentration calculations for parallel 1. $c^{exc}_{Left}$ and $c^{exc}_{Right}$ are the calculated excess density for the left and right side of the graphite.

| Component | $c^{exc}_{Left}$ | $c^{exc}_{Right}$ |
|---|---|---|
| *Electrolyte* | $2.92 * 10^{-2}$ | $1.23 * 10^{-2}$ |
| *EC* | $1.13 * 10^{-2}$ | $1.14 * 10^{-2}$ |
| *DEC* | $2.26 * 10^{-3}$ | $1.99 * 10^{-3}$ |
| *PF6-* | $1.49 * 10^{-3}$ | $3.61 * 10^{-3}$ |
| *Li+* | $1.96 * 10^{-4}$ | $3.81 * 10^{-4}$ |

Table 5: Excess Concentration calculations for parallel 2. $c^{exc}_{Left}$ and $c^{exc}_{Right}$ are the calculated excess density for the left and right side of the graphite.

| Component | $c^{exc}_{Left}$ | $c^{exc}_{Right}$ |
|---|---|---|
| *EC* | $1.83 * 10^{-3}$ | $1.28 * 10^{-2}$ |
| *DEC* | $1.86 * 10^{-1}$ | $1.73 * 10^{-1}$ |
| *PF6-* | $1.49 * 10^{-3}$ | $8.01 * 10^{-4}$ |
| *Li+* | $-3.47 * 10^{-3}$ | $-1.41 * 10^{-3}$ |

Table 6: Excess Concentration calculations for parallel 3. $c^{exc}_{Left}$ and $c^{exc}_{Right}$ are the calculated excess density for the left and right side of the graphite.

| Component | $c^{exc}_{Left}$ | $c^{exc}_{Right}$ |
|---|---|---|
| *EC* | $-3.42 * 10^{-4}$ | $1.05 * 10^{-2}$ |
| *DEC* | $2.24 * 10^{-3}$ | $-1.11 * 10^{-3}$ |
| *PF6-* | $4.43 * 10^{-3}$ | $-2.71 * 10^{-3}$ |
| *Li+* | $1.09 * 10^{-4}$ | $-4.15 * 10^{-4}$ |

The results shows that there exists a surface excess of electrolyte of $2.92 * 10^{-2}$ atom per $\mathring{A}^3$ and $1.23 * 10^{-2}$ atom/$\mathring{A}^3$ of the left and right side of the graphite interface respectively. The values of each component show more variation. Positive excess surface density of both Li+ and PF6-, was found i parallel 1. In general the surface excess was highest for the solvent. The concentration of the ions were more variable and there was also deficiency (negative values) in parallel 2 and 3. In these calculations the concentrations was calculated over a relatively large area, it could be more interesting to calculate the excess densities of the ions in each of the higher peaks instead of the whole interface region. The higher peaks of PF6-, can indicate the presence of an EDL layer, but this needs to be further investigated.

## 4.3 Lithium Intercalation

There was not seen any intercalation of Lithium ions into the graphite. Still, there was observed high peak concentrations of Li+ close to the graphite. This was also observed in Ovito (see figure 4.22). A longer production time to allow the system to evolve over an extended period of time, would be useful. This could hopefully make it possible to observe lithium intercalation.

The system required a small timestep to maintain stability, this lead to long runtimes, and the simulation was run in the NPT ensamble for only 9.1 ns.

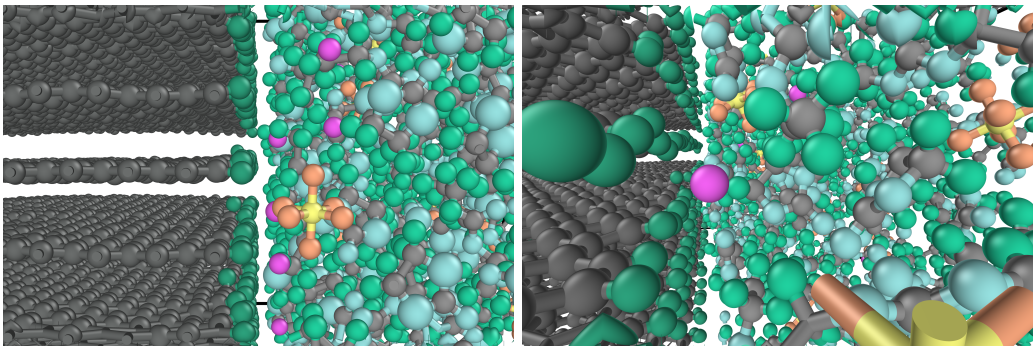

(a) (b)

Figure 4.22: Clippings from Ovito during simulation. The pink lithium ions is located in the interface close the graphite. (a) parallel 1 (b) parallel 2.

# 5 Conclusion

By accurate initialization of the graphite structure with precise force-field parameterization, constraining of the mass center, and proper equilibration, a stable model of graphite was achieved. The graphite structure, representing the anode in a lithium-ion battery, was combined with an EC-DEC electrolyte. The system demonstrated good stability and expected behaviour.

The density profile of the system was computed and the concentration of the chemical species including EC, DEC, Li+ and PF6- was recorded. The density profile of the system showed that the interface region extends about 10 Å out into the electrolyte on both sides of the graphite. Surface excess densities of the electrolyte was calculated to $2.92 * 10^{-2}$ atom/$\mathring{A}^3$ and $1.23 * 10^{-2}$ atom/$\mathring{A}^3$ at each of the interfaces of the graphite. A trend of EC-molecules and lithium ions located in higher concentrations near the graphite anode was observed. No intercalation of lithium ions into the graphite was observed during these simulations.

# 6 Future Work

The main part of this project was dedicated to construction of the MD model. Although the construction of the electrode-electrolyte model was successful, some improvements should be performed to achieve more reliable results. To gain a better representation of the bulk-electrolyte, more electrolyte should be applied at both sides of the electrolyte. The bulk density should also be calculated for all three parallels (at least). It could also be useful to plot density profiles for different time steps and even run some longer simulations. In general, more time should be used on analysing the data from the density measurements.

The intercalation of lithium ions should be further investigated. In this project a simulation time of 9.1 ns was performed in the NPT ensemble. Increasing temperature and use of longer run times can be parameters to adjust. If no intercalation is observed, other simulation techniques should be considered.

After improvements of the model a natural next step could be computing of the heat transport and recording of the temperature gradient in the system, like described in section 2.2.3. Combined with the density profiles the resistance across the interface can be determined, which can give important insights.

# References


[1] Jakob Fleischmann et al. *Battery 2030: Resilient, sustainable, and circular*. Tech. rep. McKinsey & Company, Jan. 2023. URL: https://www.mckinsey.com/industries/automotive-and-assembly/our-insights/battery-2030-resilient-sustainable-and-circular#/.

[2] Da Deng. 'Li-ion batteries: basics, progress, and challenges'. In: *Energy Science & Engineering* 3.5 (2015). _eprint: https://onlinelibrary.wiley.com/doi/pdf/10.1002/ese3.95, pp. 385–418. DOI: https://doi.org/10.1002/ese3.95. URL: https://onlinelibrary.wiley.com/doi/abs/10.1002/ese3.95.

[3] Sandeep Dhameja. '1 - Electric Vehicle Batteries'. In: *Electric Vehicle Battery Systems*. Ed. by Sandeep Dhameja. Woburn, 2002, pp. 1–21. DOI: 10.1016/B978-075069916-7/50001-7.

[4] Jia-Lin Tsai and Jie-Feng Tu. 'Characterizing mechanical properties of graphite using molecular dynamics simulation'. In: *Materials & Design* 31.1 (2010), pp. 194–199. DOI: 10.1016/j.matdes.2009.06.032.

[5] Daan Frenkel and Berend Smit. *Understanding Molecular Simulation: From Algorithms to Applications*. Second. Vol. 1. Computational Science Series. San Diego: Academic Press, 2002.

[6] H. Fehske, R. Schneider and A. Weiße. *Computational Many-Particle Physics*. Lecture Notes in Physics. Springer Berlin Heidelberg, 2007. ISBN: 978-3-540-74686-7. URL: https://link.springer.com/book/10.1007/978-3-540-74686-7.

[7] A.R. Leach. *Molecular Modelling: Principles and Applications*. Prentice Hall, 2001. ISBN: 978-0-582-38210-7.

[8] Sandia Corporation. LAMMPS Documentation: 4.6. How a timestep works. Available from: https://docs.lammps.org/Developer_flow.html. n.d.

[9] Michael Griebel. *Numerical simulation in molecular dynamics numerics, algorithms, parallelization, applications*. eng. Texts in computational science and engineering ; 5. Publication Title: Numerical simulation in molecular dynamics numerics, algorithms, parallelization, applications. Berlin, Heidelberg: Springer Berlin Heidelberg, 2007. ISBN: 978-3-540-68095-6.

[10] Mark E Tuckerman et al. 'A Liouville-operator derived measure-preserving integrator for molecular dynamics simulations in the isothermal–isobaric ensemble'. In: *JOURNAL OF PHYSICS A: MATHEMATICAL AND GENERAL* (24th Apr. 2006). DOI: 10.1088/0305-4470/39/19/S18.

[11] Sandia Corporation. LAMMPS Documentation: 8.2.4. Thermostats. Available from: https://docs.lammps.org/fix_nh.html. n.d.

[12] University of Illinois at Urbana-Champaign. Internal coordinates for bonded interactons. Available from: https://www.ks.uiuc.edu/Training/Tutorials/namd/namd-tutorial-unix-html/node25.html. n.d.

[13] M.A. González. *Force fields and molecular dynamics simulations*. 2011. DOI: 10.1051/sfn/201112009.

[14] Signe Kjelstrup and Dick Bedeaux. Non-Equilibrium Thermodynamics of Heterogeneous Systems. Vol. 16. World Scientific Publishing Co. Pte. Ltd., 2008. ISBN: 13 978-981-277-913-7.

[15] Ross Taylor and R Krishna. *Multicomponent Mass Transfer*. Wiley series in chemical engineering. Wiley, Dec. 1993.

[16] Jianzhong Wu. 'Understanding the Electric Double-Layer Structure, Capacitance, and Charging Dynamics'. In: *Chemical Reviews* 122.12 (2022), pp. 10821–10859. DOI: 10.1021/acs.chemrev.2c00097. URL: https://doi.org/10.1021/acs.chemrev.2c00097.

[17] University of Cambridge - Department of Chemical Engineering and Biotechnology. *The Electrical Double Layer*. URL: https://www.ceb.cam.ac.uk/research/groups/rg-eme/Edu/the-electrical-double-layer.

[18] Qisheng Wu, Matthew T. McDowell and Yue Qi. 'Effect of the Electric Double Layer (EDL) in Multicomponent Electrolyte Reduction and Solid Electrolyte Interphase (SEI) Formation in Lithium Batteries'. In: *Journal of the American Chemical Society* 145.4 (2023). _eprint: https://doi.org/10.1021/jacs.2c11807, pp. 2473–2484. DOI: 10.1021/jacs.2c11807. URL: https://doi.org/10.1021/jacs.2c11807.

[19] Aiping Wang et al. 'Review on modeling of the anode solid electrolyte interphase (SEI) for lithium-ion batteries'. In: *npj Computational Materials* 4.1 (Mar. 2018), p. 15. ISSN: 2057-3960. DOI: 10.1038/s41524-018-0064-0. URL: https://doi.org/10.1038/s41524-018-0064-0.

[20] A. P. Thompson et al. 'LAMMPS - a flexible simulation tool for particle-based materials modeling at the atomic, meso, and continuum scales'. In: *Comp. Phys. Comm.* 271 (2022), p. 108171. DOI: 10.1016/j.cpc.2021.108171.

[21] Aidan P. Thompson et al. 'LAMMPS - a flexible simulation tool for particle-based materials modeling at the atomic, meso, and continuum scales'. In: *Computer Physics Communications* 271 (2022), p. 108171. ISSN: 0010-4655. DOI: https://doi.org/10.1016/j.cpc.2021.108171.

[22] Magnus Själander et al. *EPIC: An Energy-Efficient, High-Performance GPGPU Computing Research Infrastructure*. 2022. arXiv: 1912.05848 [cs.DC].

[23] Alexander Stukowski. 'Visualization and analysis of atomistic simulation data with OVITO-the Open Visualization Tool'. In: *MODELLING AND SIMULATION IN MATERIALS SCIENCE AND ENGINEERING* 18.1 (JAN 2010). DOI: {10.1088/0965-0393/18/1/015012}.

[24] Sandia Corporation. LAMMPS Documentation: pair$_s tyle line / l j command$. Available from: https://docs.lammps.org/pair_lj.html. n.d.

[25] Astrid Puntervold. 'Molecular Dynamics Simulation of the Graphite Anode in Lithium-Ion Batteries'. Specialization project. Dec. 2022.

[26] William L. Jorgensen and Julian Tirado-Rives. 'Potential energy functions for atomic-level simulations of water and organic and biomolecular systems'. In: *Proceedings of the National Academy of Sciences* 102.19 (2005), pp. 6665–6670. DOI: 10.1073/pnas.0408037102.

[27] Leela S. Dodda et al. '1.14*CM1A-LBCC: Localized Bond-Charge Corrected CM1A Charges for Condensed-Phase Simulations'. In: *The Journal of Physical Chemistry B* 121.15 (20th Apr. 2017), pp. 3864–3870. DOI: 10.1021/acs.jpcb.7b00272.

[28] Leela S. Dodda et al. 'LigParGen web server: an automatic OPLS-AA parameter generator for organic ligands'. In: *Nucleic Acids Research* 45 (W1 Apr. 2017), W331–W336. DOI: 10.1093/nar/gkx312.

# Appendix A

## Force Field Parameters for Terminated Graphite

The parameters are selected by use of LiParGen (Parameter Generator for Organic Ligands) [26, 27, 28].

**Atom codes:**

C = Carbon
C* = Carbon at edge (bonded to hydrogen)
H = Hydrogen

**Pairwise force field coefficients:**
(LAMMPS pair style: LJ/cut)

| *Atom pair* | $\epsilon$ | $\sigma$ |
|---|---|---|
| C-C | 0.066047 | 3.40 |
| H-H | 0.0300 | 2.42 |

**Bond force field coefficients:**
(LAMMPS bond style: harmonic)

| *Atoms* | $K_r$ | $r_{eq}$ |
|---|---|---|
| C-C | 520 | 1.40 |
| C-C* | 469 | 1.40 |
| C-H | 367 | 1.09 |

**Angle force field coefficients:**
(LAMMPS angle style: harmonic)

| *Atoms* | $K_\theta$ | $\theta_{eq}$ |
|---|---|---|
| C-C-C | 85 | 117.3 |
| C-C-H | 35 | 120.0 |
| C-C*-C* | 63 | 120 |

**Dihedral force field coefficients:**
(LAMMPS dihedral style: OPLS)

| *Atoms* | $K_1$ | $K_2$ | $K_3$ | $K_4$ |
|---|---|---|---|---|
| All | 0 | 7.250 | 0 | 0 |

**Improper force field coefficients:**
(LAMMPS improper style: CVFF)

CVFF improper potential has the functional form:
$E = K[1 + dcos(n\phi)]$

| *Atoms* | $K$ | $d$ | $n$ |
|---|---|---|---|
| All | 2.500 | -1 | 2 |

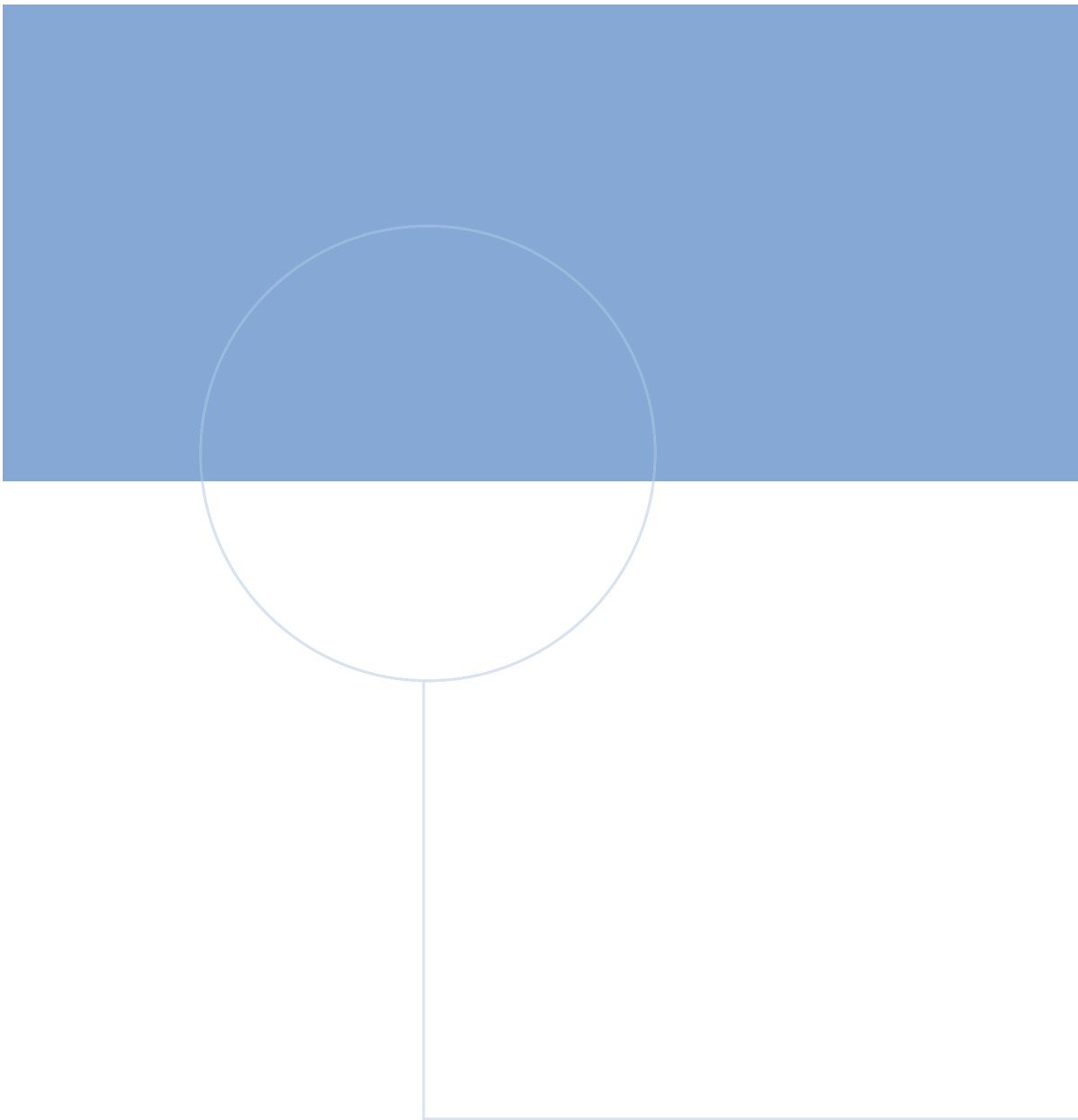

NTNU

Norwegian University of
Science and Technology